# Bow shocks, bow waves, and dust waves. III. Diagnostics

William J. Henney & S. J. Arthur

*Instituto de Radioastronomía y Astrofísica, Universidad Nacional Autónoma de México, Apartado Postal 3-72, 58090 Morelia, Michoacán, México*

**ABSTRACT**

Stellar bow shocks, bow waves, and dust waves all result from the action of a star's wind and radiation pressure on a stream of dusty plasma that flows past it. The dust in these bows emits prominently at mid-infrared wavelengths in the range $8\,\mu m$ to $60\,\mu m$. We propose a novel diagnostic method, the $\tau$–$\eta$ diagram, for analyzing these bows, which is based on comparing the fractions of stellar radiative energy and stellar radiative momentum that is trapped by the bow shell. This diagram allows the discrimination of radiation-supported bows from wind-supported bows. For the latter, it allows the stellar wind mass loss rate to be determined. We critically compare our method with a previous method that has been proposed for determining wind mass loss rates from bow shock observations. We find that the dust emissivity model used previously needs to be corrected to account for differences in the spectral energy distribution between OB stars and the interstellar radiation field, which results in a downward revision by a factor of two in the mass loss rates. After correction, the methods complement one another to some degree, with differing sensitivities to systematic model uncertainties. We point out that observations of bows are of limited utility in constraining mass loss rates of weak-wind stars, since these tend to have radiation-supported bows, which yield only upper limits to the mass loss rate.

**Key words:** circumstellar matter – radiation: dynamics – stars: winds, outflows

## 1 INTRODUCTION

In Henney & Arthur (2019a,b, Paper I and Paper II) we presented a taxonomy of stellar bows, which we divided into wind-supported bow shocks (WBS) and various classes of radiation-supported bows. When the dust and gas remains well-coupled (Paper I), these are optically thin radiation-supported bow waves (RBW) and optically thick radiation-supported bow shocks (RBS). When the dust decouples from the gas (Paper II), one has inertia-confined dust waves (IDW) and drag-confined dust waves (DDW).

In Paper I we derived expressions for the bow radius $R_0$ in each of the three well-coupled regimes as a function of the parameters of the star and the ambient medium. In Paper II, we found the criteria for the dust to decouple from the gas to form a separate dust wave outside of the hydrodynamic bow shock. The most important of these is that the ratio of radiation pressure to gas pressure should exceed a critical value, $\Xi_\dagger \sim 1000$.

In order to provide an empirical anchor to our theoretical calculations, we now consider how the parameters of our models might be determined from observations. The parameter-space diagrams, such as Figure 2 of Paper I, are not always useful in this regard, since in many cases the ambient density and relative stellar velocity are not directly measured. Instead, we aim to construct diagnostics based on the most common observations, which are of the infrared dust emission. Key questions that we wish to address include

1. Can we distinguish observationally between radiation support (bow waves and dust waves) and wind support (bow shocks)?

2. Are there any clear examples of sources with radiation-supported bows?

3. In the case of wind support, can we reliably determine mass loss rates from mid-infrared observations?

The outline of the paper is as follows. In § 2 we describe how the optical depth and the gas pressure in the bow shell can be estimated from a small number of observed quantities. In § 3 we place observed bow sources on a diagnostic diagram of these two quantities and discuss the influence of observational errors and systematic model uncertainties. In § 4 we use the diagram to identify some candidates for radiation-supported bows. In § 5 we calculate the grain emissivity as a function of the stellar radiation field around OB stars. In § 6 we compare two different methods of estimating the stellar wind mass loss rates from observations of the bows. In § 7 we summarise out findings.

## 2 OPTICAL DEPTH AND PRESSURE OF THE BOW SHELL

A fundamental parameter is the optical depth, $\tau$, of the bow shell to UV radiation, which determines what fraction of the stellar photon momentum is available to support the shell (see § 2.1 of Paper I). But the same photons also heat the dust grains in the bow, which re-radiate that energy predominantly at mid-infrared wavelengths (roughly $10\,\mu m$ to $100\,\mu m$) with luminosity $L_{\mathrm{IR}}$. Assuming that Ly$\alpha$ and mechanical heating of the dust shell is negligible (see § 5.1) and
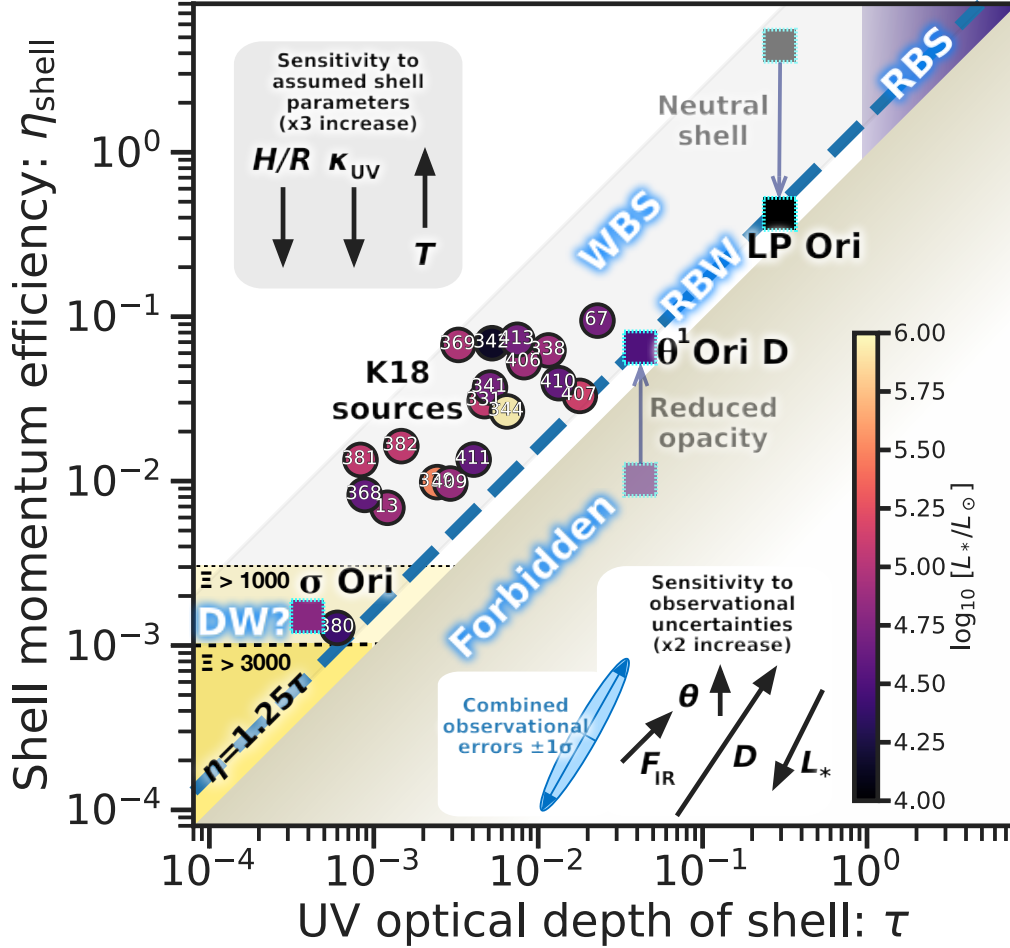
**Figure 1.** Observational diagnostic diagram for bow shocks. The shell optical depth $\tau$ ($x$ axis) and momentum efficiency $\eta_{\rm sh}$ ($y$ axis) can be estimated from observations of the bolometric stellar luminosity, infrared shell luminosity, and shell radius, as described in the text. Results are shown for the 20 sources (circle symbols) from Kobulnicky et al. (2018) plus three further sources (square symbols), where we have obtained the measurements ourselves (see Tab. 1). The color of each symbol indicates the stellar luminosity (dark to light) as indicated by the scale bar. The shell pressure is determined assuming a gas temperature $T = 10^4$ K, an absorption opacity $\kappa = 600\,{\rm cm^2\,g^{-1}}$, and a thickness-to-radius ratio $H/R = 0.25$. The sensitivity of the results to a factor-of-three change in each parameter is shown in the upper inset box. Exceptions are the two Orion Nebula sources, $\theta^1$ Ori D and LP Ori, where the small dim squares show the results of assuming the standard shell parameters, while the large squares show the results of modifications according to the peculiar circumstances of each object, as described in the text. The lower inset box shows the sensitivity of the results to a factor-of-two uncertainty in each observed quantity: distance to source $D$; stellar luminosity $L_*$, shell infrared flux $F_{\rm IR}$; shell angular size $\theta$. Lines and shading indicate different theoretical bow regimes (see Paper I and Paper II). The dashed blue diagonal line corresponds to radiation-supported bows, while the upper left region corresponds to wind-supported bows. The upper right corner (purple) corresponds to optically thick bow shocks, while the lower left corner (yellow) is the region where grain–gas separation *may* occur, leading to a potential dust wave. However, the existence of a dust wave in this region is not automatic, since it only includes one of the four necessary conditions (§§ 4.4 and 5.1 of Paper II). The lower-right region is strictly forbidden, except in case of violation of the assumption that dust heating be dominated by stellar radiation.

that the emitting shell subtends a solid angle $\Omega$, as seen from the star, then the optical depth can be estimated as

$$\tau = -\ln\left(1 - \frac{4\pi}{\Omega}\frac{L_{\rm IR}}{L_*}\right) \approx \frac{2L_{\rm IR}}{L_*}\,, \qquad (1)$$

where the last approximate equality holds if $\tau \ll 1$ and the shell emission covers one hemisphere. Note that the $\tau$ of Paper I is not exactly the same as the $\tau$ of equation (1), but is larger by a factor of $Q_P/Q_{\rm abs} = 1 + \varpi(1-g)/(1-\varpi)$, where $\varpi$ is the grain albedo and $g$ the scattering asymmetry. This is plotted in Figure 6a of Paper II

for Cloudy's default ISM grain mixture (see § 5 below), where it can be seen that $Q_P/Q_{\rm abs} = 1.2$ to $1.3$ at EUV/FUV wavelengths ($\lambda = 0.05\,\mu{\rm m}$ to $0.2\,\mu{\rm m}$), so the correction is small.

A second important parameter is the thermal plus magnetic pressure in the shocked shell, which is doubly useful since in a steady state it is equal to *both* the internal supporting pressure (wind ram pressure plus absorbed stellar radiation) *and* the external confining pressure (ram pressure of ambient stream). The shell pressure is not given directly by the observations, but can be determined by the following three steps:

**Table 1.** Key observational parameters for star/bow systems

| Star | $L_*/\mathrm{L}_\odot$ | $L_{\mathrm{IR}}/\mathrm{L}_\odot$ | $R_0/\mathrm{pc}$ |
|---|---|---|---|
| $\theta^1$ Ori D | $2.95 \times 10^4$ | 620 | 0.003 |
| LP Ori | 1600 | 240 | 0.01 |
| $\sigma$ Ori | $6 \times 10^4$ | 15 | 0.12 |
| K18 Sources | $1.4 \times 10^4$ to $8.7 \times 10^5$ | 8 to 2800 | 0.02 to 1.35 |

P1. The shell mass column ($\mathrm{g\,cm^{-2}}$) can be estimated from the optical depth by assuming an effective UV opacity: $\Sigma_{\mathrm{sh}} = \tau/\kappa$

P2. The shell density ($\mathrm{g\,cm^{-3}}$) can be found from the mass column if the shell thickness is known: $\rho_{\mathrm{sh}} = \Sigma/h_{\mathrm{sh}}$. In the absence of other information, a fixed fraction of the shell radius can be used. In particular, we normalize by a typical value of one quarter the star–apex distance: $h_{1/4} = h_{\mathrm{sh}}/(0.25R_0)$. This corresponds to a Mach number $\mathcal{M}_0 = \sqrt{3}$ if the stream shock is radiative, or $\mathcal{M}_0 \gg 1$ if non-radiative (see § 3.2 of Paper I). Further discussion is given in § 6.2 below.

P3. Finally, the pressure ($\mathrm{dyne\,cm^{-2}}$) follows by assuming values for the sound speed and Alfvén speed: $P_{\mathrm{sh}} = \rho_{\mathrm{sh}}(c_{\mathrm{s}}^2 + \frac{1}{2}v_{\mathrm{A}}^2)$.

It is natural to normalize this pressure to the stellar radiation pressure at the shell, so we define a shell momentum efficiency

$$\eta_{\mathrm{sh}} \equiv \frac{P_{\mathrm{sh}}}{P_{\mathrm{rad}}} = \frac{4\pi R_0^2 \left(c_{\mathrm{s}}^2 + \frac{1}{2}v_{\mathrm{A}}^2\right)\tau}{L_* \kappa h_{\mathrm{sh}}} \approx 245 \frac{R_{\mathrm{pc}} T_4 \tau}{L_4 \kappa_{600} h_{1/4}}, \quad (2)$$

where in the last step we have assumed ionized gas with negligible magnetic support ($v_{\mathrm{A}} \ll c_{\mathrm{s}}$) and written the stellar luminosity and shell parameters in terms of typical values, which we summarize below. Note that the shell momentum efficiency is simply the reciprocal of the radiation parameter from Paper II's equation (23): $\eta_{\mathrm{sh}} = \Xi_{\mathrm{sh}}^{-1}$, which provides yet a third use for $\eta_{\mathrm{sh}}$, since $\Xi$ is paramount in determining whether the grains and gas remain well-coupled (see § 4.4 of Paper II).

In this section and the remainder of the paper, we employ dimensionless versions of the stellar bolometric luminosity, $L_*$, wind mass-loss rate, $\dot{M}$, and terminal velocity, $V_{\mathrm{w}}$, together with the ambient stream's mass density, $\rho$, relative velocity $v_\infty$, and effective dust opacity, $\kappa$. These are defined as follows:

$$\dot{M}_{-7} = \dot{M}/\left(10^{-7}\,\mathrm{M}_\odot\,\mathrm{yr}^{-1}\right)$$
$$V_3 = V_{\mathrm{w}}/\left(1000\,\mathrm{km\,s}^{-1}\right)$$
$$L_4 = L_*/\left(10^4\,\mathrm{L}_\odot\right)$$
$$v_{10} = v_\infty/\left(10\,\mathrm{km\,s}^{-1}\right)$$
$$n = (\rho/\bar{m})/\left(1\,\mathrm{cm}^{-3}\right)$$
$$\kappa_{600} = \kappa/\left(600\,\mathrm{cm}^2\,\mathrm{g}^{-1}\right),$$

where $\bar{m}$ is the mean mass per hydrogen nucleon ($\bar{m} \approx 1.3m_{\mathrm{p}} \approx 2.17 \times 10^{-24}$ g for solar abundances).

## 3 THE $\eta_{\mathrm{sh}}$–$\tau$ DIAGNOSTIC DIAGRAM

In Figure 1 we show the resultant diagnostic diagram: $\eta_{\mathrm{sh}}$ versus $\tau$. The horizontal axis shows the fraction of the stellar radiative *energy* that is reprocessed by the bow shell, while the vertical axis shows the fraction of stellar radiative *momentum* that is imparted to the shell, either directly by absorption, or indirectly by the stellar wind (which is itself radiatively driven). Radiatively supported bows (DW, RBW, or RBS, or cases) should lie on the diagonal

line $\eta_{\mathrm{sh}} = (Q_P/Q_{\mathrm{abs}})\tau \approx 1.25\tau$, where we have used the ratio of grain radiation pressure efficiency to absorption efficiency found in the FUV band for the dust mixture shown in Paper II's Figure 6. Wind-supported bows should lie above this line and no bows should lie below the $\eta_{\mathrm{sh}} = \tau$ line, since $Q_P$ cannot be smaller than $Q_{\mathrm{abs}}$.

We have calculated $\eta_{\mathrm{sh}}$ and $\tau$ using the above-described methods for the 20 mid-infrared sources studied by Kobulnicky et al. (2018) (K18) and plotted them on our diagnostic diagram. Details of our treatment of this observational material are provided in the following subsection. In order to expand the range of physical conditions, we have included three additional sources (data in Table 1): bows around $\theta^1$ Ori D (Smith et al. 2005) and LP Ori (O'Dell 2001) in the Orion Nebula, which show larger optical depths, plus the inner bow around $\sigma$ Ori, which illuminates the Horsehead Nebula and has previously been claimed to be a dust wave (Ochsendorf et al. 2014; Ochsendorf & Tielens 2015). Details of the observations of these additional sources will be published elsewhere.

### 3.1 Treatment of sources from Kobulnicky et al.

In a series of papers Kobulnicky et al. provide an extensive mid-infrared-selected sample of over 700 candidate stellar bow shock nebulae (Kobulnicky et al. 2016, 2017, 2018, hereafter K16, K17, and K18). For 20 of these sources, reliable distances and spectral classifications are provided in Table 5 of K17 and Tables 1 and 2 of K18. In this section, we outline how we obtain $\tau$ and $\eta_{\mathrm{sh}}$ from the data in these catalogs, while further aspects of the Kobulnicky et al. material are discussed in § 6.2.

The UV optical depth of the bow shell is obtained (eq. [1]) from the ratio of infrared shell luminosity to stellar luminosity. The inverse of this ratio is given in Table 5 of K17, but we choose to re-derive the values since the spectral classification of some of the sources was revised between K17 and K18. Although K17 found the total shell fluxes from fitting dust emission models to the observed SEDs, we adopt the simpler approach of taking a weighted sum of the flux densities $F_\nu$ (in Jy) in three mid-infrared bands:

$$F_{\mathrm{IR}} \approx \left[2.4\,(F_8\text{ or }F_{12}) + 1.6\,(F_{22}\text{ or }F_{24})\right.$$
$$\left. + 0.51\,F_{70}\right] \times 10^{-10}\,\mathrm{erg\,s}^{-1}\,\mathrm{cm}^{-2}, \quad (3)$$

where $F_8$ is Spitzer IRAC 8.0 µm, $F_{24}$ is Spitzer MIPS 23.7 µm, $F_{12}$ and $F_{22}$ are WISE bands 3 and 4, and $F_{70}$ is Herschel PACS 70 µm. The weights are chosen so that the integral $\int_0^\infty F_\nu\,d\nu$ is approximated by the sum $\Sigma_k F_k\,\Delta\nu_k$, under the assumption that fluxes in shorter (e.g., IRAC 5.8 µm) and longer (e.g., PACS 150 µm) wavebands are negligible. Shell fluxes are converted to luminosities using the assumed distance to each source, and stellar luminosities are taken directly from K18 Table 2, based on spectroscopic classification and the calibrations of gravity and effective temperature from Martins et al. (2005).

In Figure 2 we compare the $\tau$ obtained using the shell luminosity as described above with that obtained using the luminosity ratios directly from K17 Table 5. It can be seen that for the majority of sources the two measurements are consistent within a factor of two (gray band). The four furthest-flung outliers can be understood as follows:

*Source 67* This has a very poor-quality spectral fit in K17 (see lower left panel of their Fig. 12) and so $F_{\mathrm{IR}}$ is overestimated by them by a factor of 10.

*Sources 341 and 342* The spectral classes changed from B2V in K17 to O9V and B1V, respectively, in K18, increasing the derived $L_*$, which lowers $\tau$.
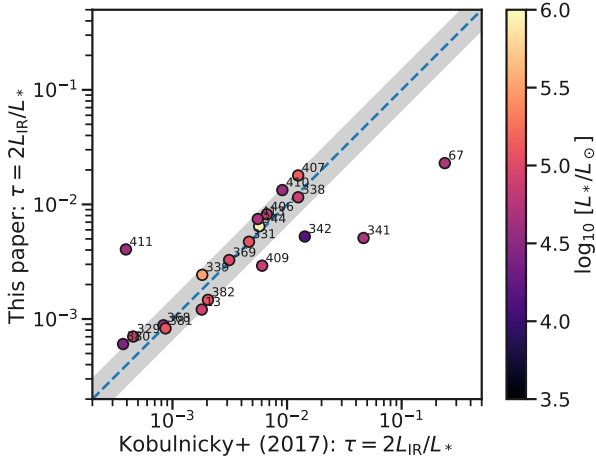
**Figure 2.** Comparison between shell-to-star luminosity ratios calculated as described in the text ($y$ axis) with those given in K17 ($x$ axis). The blue dashed line signifies equality and the gray band shows ratios between 1/2 and 2.

*Source 411* The luminosity class changed from Ib (K17) to V (K18), so $L_*$ has been greatly reduced, which increases $\tau$.

### 3.2    Random uncertainties due to observational errors

The fundamental observational quantities that go into determining $\tau$ and $\eta_{sh}$ for each source are distance, $D$; stellar luminosity, $L_*$; total infrared flux, $F_{IR}$; and bow angular apex distance, $\theta$. From these, the shell radius and infrared luminosity are found as $R_0 = \theta D$ and $L_{IR} = 4\pi D^2 F_{IR}$. Rather than clutter the diagram with error bars, we instead show the sensitivity to observational errors in the lower-right box, where each arrow corresponds to a factor of two increase (0.3 dex) in each quantity: $D$, $L_*$, $F_{IR}$, and $\theta$. We now calculate uncertainty estimates for individual observational quantities that are used in deriving not only $\tau$ and $\eta_{sh}$, but also mass-loss rates, as discussed later in § 6.

#### 3.2.1    Distance

Most sources are members of known high-mass clusters with distance uncertainties less than 20% (0.08 dex). The only exception is Source 329 in Cygnus, for which the distance uncertainty is roughly a factor of 2 (Kobulnicky et al. 2018).

#### 3.2.2    Stellar luminosity

The stellar luminosity is determined from spectral classification, which makes it independent of distance. Taking a 2000 K dispersion in the effective temperature scale (Martins et al. 2005) gives an uncertainty of 25% in the luminosity, and adding in possible errors in gravity and the effect of binaries, we estimate a total uncertainty in $L_*$ of 50% (0.45 mag or 0.18 dex).

#### 3.2.3    Shell flux and surface brightness

We estimate the uncertainty in shell bolometric flux, $F_{IR}$, by comparing two different methods: model fitting (Kobulnicky et al. 2017)

and a weighted sum of the 8, 24, and 70 μm bands (eq. [3]), giving a standard deviation of 17% (0.07 dex). To this, we add the estimate of 25% for the effects of background subtraction uncertainties on individual photometric measurements (Kobulnicky et al. 2017). The absolute flux calibration uncertainty for both Herschel PACS (Balog et al. 2014) and Spitzer MIPS (Engelbracht et al. 2007) is less than 5%, which is small in comparison. Combining the 3 contributions in quadrature gives a total uncertainty of 0.12 dex. We adopt the same uncertainty for the 70 μm surface brightness.

#### 3.2.4    Angular sizes

For the angular apex distance, $\theta$, the largest uncertainty for well-resolved sources is due to the unknown inclination. Tarango-Yong & Henney (2018) show that the dispersion in true to projected distances can introduce an uncertainty of 30% (0.11 dex) in unfavorable cases (e.g., their Fig. 26). For 5 of the 20 sources from Kobulnicky et al. (2018), $\theta$ is of order the Spitzer PSF width at 24 μm, so the errors may be larger.

#### 3.2.5    Stellar wind velocity

Although this is not strictly an observed quantity for the K18 sample, we will treat it as such since it is estimated per star, based on the spectral type. K18 estimate 50% uncertainty, and we adopt the same here (0.18 dex).

#### 3.2.6    Combined effect of uncertainties on the $\tau$–$\eta_{sh}$ diagram

Assuming that the uncertainty in each observational quantity is independent, we can now combine them using the techniques described in Appendix A to find the $\pm 1\,\sigma$ error ellipse, shown in blue in the figure. It can be seen that observational uncertainties in $\tau$ and $\eta_{sh}$ are highly correlated: the dispersion is 0.7 dex in the product $\eta_{sh}\tau$ but only 0.16 dex in the ratio $\eta_{sh}/\tau$, with stellar luminosity errors dominating in both cases. Observational uncertainties are therefore relatively unimportant in determining whether a given source is wind-driven or radiation-driven, which depends only on $\eta_{sh}/\tau$. On the other hand, they do significantly effect the question of whether a source has a sufficiently high radiation parameter $\Xi$ to possibly be a dust wave.

### 3.3    Systematic uncertainties due to assumed shell parameters

A further source of uncertainty arises from the parameters of the shocked shell that are assumed in steps P1–P3. Namely, the relative shell thickness, $h_{sh}/R_0$, the ultraviolet grain opacity per mass of gas, $\kappa$, and the shell temperature, $T$. These parameters effect only $\eta_{sh}$, not $\tau$, with a sensitivity shown by arrows in the upper left box of Figure 1.

#### 3.3.1    Shell thickness

We do not expect a great deal of variation in the shell thickness, except for in the case of fast runaway stars ($v > 100\,\mathrm{km\,s^{-1}}$), for which the shell may be dramatically thinner if the post-shock cooling is sufficiently rapid ($h/R_0 \sim M_0^{-2}$). For ambient densities less than about $10\,\mathrm{cm^{-3}}$, the minimum thickness is about ten times smaller than we are assuming. This occurs at $v \approx 60\,\mathrm{km\,s^{-1}}$, corresponding to the peak in the cooling curve at $10^5$ K (see § 3.2 of Paper I), since the thickness is set by the cooling length at higher speeds.

In principle, the shell thickness can be measured observationally if the source is sufficiently well resolved (Kobulnicky et al. 2017), although this is complicated by projection effects.

### 3.3.2 *Dust opacity*

The dust opacity will depend on the total dust-gas ratio and on the composition and size distribution of the grains. Our adopted value of $600\,\mathrm{cm^2\,g^{-1}}$, or $1.3 \times 10^{-21}\,\mathrm{cm^2\,H^{-1}}$, is appropriate for average Galactic interstellar grains in the EUV and FUV (e.g., Weingartner & Draine 2001), but there is ample evidence for substantial spatial variations in grain extinction properties (Fitzpatrick & Massa 2007), both on Galactic scales (Schlafly et al. 2016) and within a single star forming region (Beitia-Antero & Gómez de Castro 2017). The properties of grains within photoionized regions are very poorly constrained observationally because the optical depth is generally much lower than in overlying neutral material. In the Orion Nebula, there is some evidence (Salgado et al. 2016) that the FUV dust opacity in the ionized gas may be as low as $90\,\mathrm{cm^2\,g^{-1}}$, although the uncertainties in this estimate are large and different results are obtained in other regions, such as W3(A) (Salgado et al. 2012). It is even possible that the FUV dust opacity may be larger than the ISM value if the abundance of very small grains is enhanced through radiative torque disruption of larger grains (Hoang et al. 2018).

### 3.3.3 *Shell gas temperature*

For bows around O stars, the shell temperature should be close to the photoionization equilibrium value of $\approx 10^4$ K, since the post-shock cooling length is short in ambient densities above $0.1\,\mathrm{cm^{-3}}$ (§ 3.2 of Paper I) and the shell does not trap the ionization front for ambient densities below $10^4\,\mathrm{cm^{-3}}$ (§ 3.1 of Paper I). For B stars, on the other hand, these two density limits move closer together (cf. the smaller gap between the blue and red lines in Paper I's Figs. 2a and 4, as compared with 2b and c), making it more likely that a bow will lie in a different temperature regime. The only source for which we have evidence that this occurs is LP Ori, as discussed in the next section.

### 3.4 Special treatment of particular sources

For two of the additional bows listed in Table 1, we are forced to deviate from the default values for the shell parameters. For LP Ori, the bow shell appears to be formed from neutral gas (O'Dell 2001) and its relatively high $\tau$ value is more than sufficient to trap the weak ionizing photon output of a B3 star. We therefore move its point in Figure 1 downward to reflect a temperature of 1000 K (or, equivalently, a magnetically supported shell with $v_A \approx 3\,\mathrm{km\,s^{-1}}$). For the case of the Orion Trapezium star $\theta^1$ Ori D, we find that using the default parameters results in a placement well inside the forbidden zone of Figure 1 (indicated by fainter symbol). For this object there is no reason to suspect anything but the usual photoionized temperature of $10^4$ K, but its placement could be resolved either by decreasing the shell thickness, or decreasing the UV dust opacity, or both. Given the moderate limb brightening seen in the highest resolution images of the Ney–Allen nebula (Robberto et al. 2005; Smith et al. 2005), the shell thickness is unlikely to be less than half our default value. But, if this were combined with a factor 5 decrease in $\kappa$, as suggested by Salgado et al. (2016), then this would be sufficient to move the source up to the RBW line, or slightly above.

## 4 CANDIDATE RADIATION-SUPPORTED BOWS

Four sources are sufficiently close to the diagonal line $\eta_{\mathrm{sh}} = 1.25\tau$ in Figure 1 that they should be treated as potential candidates for radiation-supported bows. These are K18 sources 380 (HD 53367, V750 Mon) and 407 (HD 93249 in Carina) plus $\theta^1$ Ori D and LP Ori. Of the four, source 380 is the only one that is also a candidate for grain-gas decoupling. Further details of the two K18 sources are presented in following subsections, where for source 380 we show that reducing both luminosity and distance by a factor of roughly 2 with respect to the values used by K18 would provide a better fit to the totality of observational data. However, the ratio $\eta_{\mathrm{sh}}/\tau$ is proportional to $D/L_*$ so it would not be affected by such an adjustment and the bow remains radiation-supported. On the other hand $\eta_{\mathrm{sh}}$ (proportional to $D/L_*^2$) would increase by 2, making the classification as dust wave candidate more marginal.

### 4.1 Source 380, HD 53367, V750 Mon

This is a Herbig Be star with spectral type B0V–B0III and mass 12 to $15\,\mathrm{M_\odot}$, which shows long-scale irregular photometric variability (Tjin A Djie et al. 2001; Pogodin et al. 2006) together with cyclic radial velocity variations, which are interpreted as an eccentric binary with a $5\,\mathrm{M_\odot}$ pre-main-sequence companion. It is located outside the solar circle and, although it was originally classified as part of the CMa OB association at about 1 kpc (Tjin A Djie et al. 2001), more recent estimates put it much closer. K18 assume a distance of 260 pc, based on Hipparcos measurements (van Leeuwen 2007), but its Gaia DR2 parallax (Gaia Collaboration et al. 2016, 2018; Luri et al. 2018) puts it closer still at $(140 \pm 30)\,\mathrm{pc}$.[1]

    Quireza et al. (2006b) report a kinematic distance to the associated H II region IC 2177 (G223.70–1.90) of 1.6 kpc, based an LSR radio recombination line velocity of $16\,\mathrm{km\,s^{-1}}$ (Quireza et al. 2006a) and the outer Galaxy rotation curve of Brand & Blitz (1993). However, given the dispersion in peculiar velocities of star-forming clouds ($7\,\mathrm{km\,s^{-1}}$ to $9\,\mathrm{km\,s^{-1}}$, Stark 1984) and likely streaming motions of the ionized gas ($\approx 10\,\mathrm{km\,s^{-1}}$, Matzner 2002; Lee et al. 2012), this is still consistent with a much smaller distance, which would also help in bringing the radio continuum-derived nebular electron density into agreement with the value ($\approx 100\,\mathrm{cm^{-3}}$) derived from the optical [S II] line ratio (Hawley 1978).

    Fairlamb et al. (2015) derive a distance of $(340 \pm 60)\,\mathrm{pc}$ from combining a spectroscopically determined effective temperature, gravity, and reddening with photometry and pre-main sequence evolutionary tracks. They also determine a luminosity of $(13\,000 \pm 1000)\,\mathrm{L_\odot}$, which is only half that assumed by K18, and would have to be even lower to bring the photometry into concordance with the Gaia distance. Alternatively, the luminosity could remain the same if the total-to-selective extinction ratio were higher than the $R_V = 3.1$ assumed by Fairlamb et al. (2015). Taking $R_V = 5.5$ instead, as in Orion, would give $A_V = 3.34$ and a predicted $V$ magnitude of 6.7 if we assume $L_4 = 1.3$, $D = 170$ pc (furthest distance in Gaia 90% confidence interval) and $T_{\mathrm{eff}} = 29.5$ kK (Fairlamb et al. 2015) for a bolometric correction of $-2.86$ (Nieva 2013). The observed brightness varies between $V = 6.9$ and 7.2, which is still at least 20% fainter than predicted, but this is the best that can be achieved without rejecting the Gaia parallax distance entirely.

----

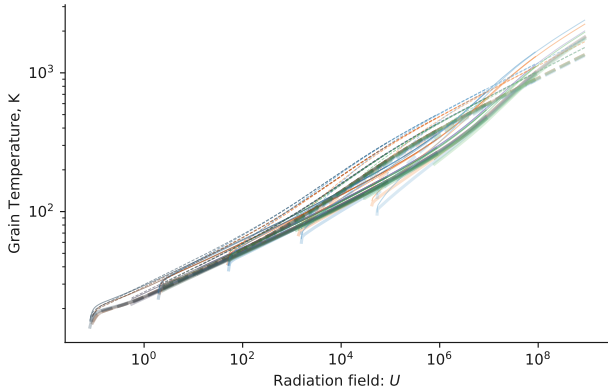[1] Median and 90% confidence interval, estimated from Bayesian inference using an exponential density distribution with scale length of 1350 pc as a prior (see https://github.com/agabrown/astrometry-inference-tutorials/).

**Figure 3.** Grain temperature versus radiation field mean intensity, $U$, in units of the interstellar radiation field in the solar neighborhood. Line types and colors correspond to a variety of stellar spectral shapes, gas densities, and grain species. Dashed lines show carbon grains, solid lines show silicate grains, with line thickness increasing and opacity decreasing with increasing grain size. Stellar spectral types are O5 V (blue), O9 V (orange), B1.5 V (purple), and B0.7 Ia (green), with lighter shades denoting higher gas densities.

A final sanity check can be performed by considering the free-free radio continuum flux of V750 Mon's surrounding H II region, which, after converting to a luminosity, should be proportional to the total recombination rate in the nebula and therefore, assuming photoionization equilibrium and negligible dust absorption in the ionized gas, also proportional to the ionizing photon luminosity of the star. Quireza et al. (2006b) report a flux density of 6 Jy at 8.6 Ghz for G223.70−1.90, as compared with a flux density of 260 Jy for the Orion Nebula using the same instrumental setup. Assuming an ionizing photon luminosity of $S_{49} = 1$ and distance 410 pc for the ionizing Trapezium stars in Orion, therefore implies $S_{49} = 0.0027(D/140\,\mathrm{pc})^2$ for V750 Mon. Using an ionizing flux of $3.2 \times 10^{22}\,\mathrm{cm}^{-2}\,\mathrm{s}^{-1}$ from the curves in Fig. 4 of Sternberg et al. (2003), this translates to a bolometric luminosity of $L_4 = 0.96(D/140\,\mathrm{pc})^2$, which is consistent with the Fairlamb et al. (2015) value if we take a distance towards the high end of the Gaia range.

## 4.2 Source 407, HD 93249

TODO

## 5 MID-INFRARED GRAIN EMISSIVITY

In preparation for our discussion of different wind mass loss diagnostic methods below, in this section we calculate the grain emissivity predicted by models of dust heated by a nearby OB star. We use the same simulations that we employed in § 4.2 of Paper II, which employ the plasma physics code Cloudy (Ferland et al. 2013, 2017). In summary, simulations of spherically symmetric, steady-state, constant density H II regions were carried out for four different stellar types from B1.5 to O5 (Table 2 of Paper II), a range of gas densities from $1\,\mathrm{cm}^{-3}$ to $10^4\,\mathrm{cm}^{-3}$, and using Cloudy's default "ISM" graphite/silicate dust mixture with 10 size bins from $0.005\,\mu\mathrm{m}$ to $0.25\,\mu\mathrm{m}$.

Figure 3 shows equilibrium grain temperatures for these Cloudy models as a function of the nominal energy density of the radiation
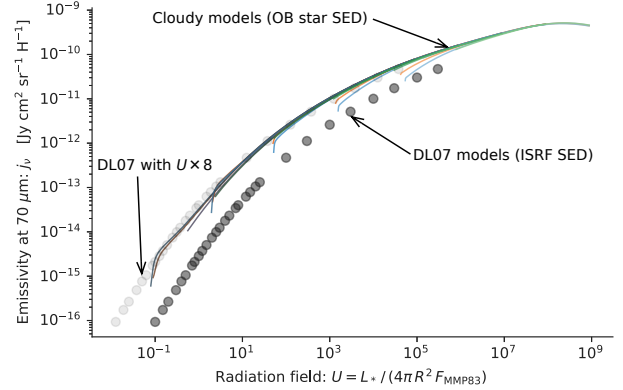


**Figure 4.** Grain emissivity at 70 μm for all Cloudy models, with lines colored as in Fig. 3, but without the variation in line type and thickness since emissivity is integrated over all grain types and sizes. For comparison, the emissivity from the grain models of Draine & Li (2007) are shown as dark gray symbols, which assume illumination by a scaled interstellar radiation field with a SED with a very different shape from that of an OB star, see Fig. 5. The light gray symbols show the effect of using an 8 times higher $U$ with the Draine & Li models, which approximately compensates for this difference in SED.

field, $U = u/u_{\mathrm{MMP83}}$, where $u = L/4\pi R^2 c$ and $u_{\mathrm{MMP83}}$ is the energy density of the interstellar radiation field for $\lambda < 8\,\mu\mathrm{m}$ in the solar neighborhood (Mathis et al. 1983):

$$u_{\mathrm{MMP83}}\, c = 0.0217\,\mathrm{erg}\,\mathrm{s}^{-1}\,\mathrm{cm}^{-2}\,. \qquad (4)$$

The tight relationship seen in Figure 3 between $T$ and $U$ is evidence for the dominance of stellar radiative heating, which we justify on theoretical grounds in § 5.1 below. The variation about the mean relation is mainly due to differences in grain size and composition, with smaller grains and graphite grains being relatively hotter. The downward hooks seen on the left end of each simulation's individual curve are due to the fact that our calculation of $U$ does not account for internal absorption, which starts to become important near the ionization front.

The grain emissivity at 70 μm (Herschel PACS blue band) for the Cloudy simulations (colored lines) is shown in Figure 4, where it is compared with the same quantity from the grain models (dark gray symbols) of Draine & Li (2007). A clear difference is seen between the two sets of models, but this is due almost entirely to a difference in the assumed spectrum of the illuminating radiation, as illustrated in Figure 5. Draine & Li (2007) use a SED that is typical of the interstellar radiation field in the Galaxy, which is dominated by an old stellar population, which peaks in the near infrared, with only a small FUV contribution from younger stars (about 8% of the total energy density). This is very different from the OB star SEDs, which are dominated by the FUV and EUV bands. Since the grain absorption opacity is substantially higher at UV wavelengths than in the visible/IR (see Fig. 6 of Paper II), the effective grain heating efficiency of the OB star SED is correspondingly higher. The light gray symbols show the effect on the Draine & Li (2007) models of multiplying the radiation field by a factor of 8 in order to offset this difference in efficiency, which can be seen to bring them into close agreement with the Cloudy models. A further difference is that the Draine & Li (2007) model includes small PAH particles, which we do not include in our Cloudy models, since they are believed to be largely absent in photoionized regions (Giard et al. 1994;
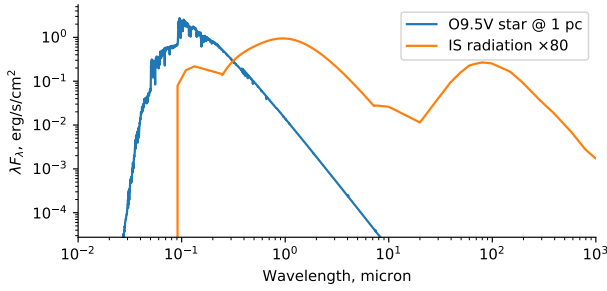
**Figure 5.** Comparison between the spectral energy distribution (SED) of a typical OB star (blue line) and the interstellar radiation field in the solar neighborhood (orange line). The OB star is the $20\,M_\odot$ model from Table **??** and is plotted for a distance from the star of 1 pc. The interstellar SED is from Mathis et al. (1983) and is multiplied by 80 so that the total FUV-to-NIR flux is equal for the two SEDs.

Lebouteiller et al. 2011). However, this only effects the emissivity at shorter mid-infrared wavelengths $< 20\,\mu m$.

In terms of the characteristic parameters introduced in § 2 the dimensionless radiation field becomes

$$U = 14.7\, L_4\, R_{\rm pc}^{-2}\,, \tag{5}$$

or, alternatively, it can be expressed in terms of the ambient stream as

$$U = 3.01\, n_\infty\, v_{10}^2 / x^2\,, \tag{6}$$

where $x = R_0/R_*$ is given by Paper I's equation (12). It can also be related to the radiation parameter $\Xi$, defined in Paper II's equation (23), as

$$U = 3.82\, n T_4\, \Xi\,. \tag{7}$$

A common alternative approach to scaling the radiation field (see Tielens & Hollenbach 1985 and citations thereof) is to normalize in the FUV band ($0.0912\,\mu m$ to $0.24\,\mu m$), where the local interstellar value is known as the Habing flux (Habing 1968):

$$F_{\rm Habing} = 0.0016\,{\rm erg\,s^{-1}\,cm^{-2}}\,. \tag{8}$$

The resultant dimensionless flux is often denoted by $G_0$, and the relationship between $G_0$ and $U$ depends on the fraction $f_{\rm fuv}$ of the stellar luminosity that is emitted in the FUV band:

$$G_0 = f_{\rm fuv}\, \frac{u_{\rm MMP83}\, c}{F_{\rm Habing}}\, U = (6\ {\rm to}\ 10)\, U\,, \tag{9}$$

where we give the range corresponding to early O ($f_{\rm fuv} \approx 0.4$) to early B ($f_{\rm fuv} \approx 0.7$) stars.

## 5.1 Unimportance of other heating mechanisms

The grain temperature in bows around OB stars is determined principally by the steady-state equilibrium between the absorption of stellar UV radiation (heating) and the thermal emission of infrared radiation (cooling). Other processes such as single-photon stochastic heating, Lyman $\alpha$ line radiation, and post-shock collisional heating can dominate in other contexts, but these are generally unimportant for circumstellar bows, as we now demonstrate.

### 5.1.1 Stochastic single-photon heating

When the radiation field is sufficiently dilute, then a grain that absorbs a photon has sufficient time to radiate all that energy away before it absorbs another photon (Duley 1973). In this case, the emitted infrared spectrum for $\lambda < 50\,\mu m$ becomes relatively insensitive of the energy density of the incident radiation (Draine & Li 2001). However, this is most important for the very smallest grains. From equation (47) of Draine & Li (2001), one finds that grains with sizes larger than $a = 0.005\,\mu m = 5\,{\rm nm}$ (the smallest size included in our Cloudy models) should be close to thermal equilibrium for $U > 30$, which is small compared with typical bow shock values ($U = 10^3$ to $10^6$). As mentioned above, PAHs are not expected to be present in the interior of H II regions. Desert et al. 1990 found them to be strongly depleted for $U > 100$ around O stars. However, other types of ultra-small grains, down to sub-nm sizes (Xie et al. 2018) may be present in bows, and stochastic heating *would* be important for grains with $a = 1\,{\rm nm}$ if $U < 10^5$. Note, however that grains smaller than $0.6\,{\rm nm}$ would be destroyed by sublimation after absorbing a single He-ionizing photon.

### 5.1.2 Lyman $\alpha$ heating

On the scale of an entire H II region, the dust heating is typically dominated by Lyman $\alpha$ hydrogen recombination line photons, which are trapped by resonant scattering (e.g., Spitzer 1978 § 9.1b). However, this is no longer true on the much smaller scale of typical bow shocks. An upper limit on the Lyman $\alpha$ energy density can be found by assuming all line photons are ultimately destroyed by dust absorption rather than escaping in the line wings (e.g., Henney & Arthur 1998), which yields

$$U_{\rm Ly\alpha} \approx 0.1 n/\kappa_{600}\,. \tag{10}$$

This can be combined with equation (6) to give the ratio of Lyman $\alpha$ to direct stellar radiation as

$$\frac{U_{\rm Ly\alpha}}{U} \approx 0.03 \frac{x^2}{v_{10}^2 \kappa_{600}}\,. \tag{11}$$

Taking the most favorable parameters imaginable of a slow stream ($v_{10} = 2$), very strong wind ($x \approx 1$), and reduced dust opacity ($\kappa_{600} = 0.1$) gives a Lyman $\alpha$ contribution of only 10% of the stellar radiative energy density. In any other circumstances, the fraction would be even lower.

### 5.1.3 Shock heating

The outer shock thermalizes the kinetic energy of the ambient stream, which may in principle contribute to the infrared emission of the bow. In order for this process to be competitive, the following three conditions must all hold:

1. The post-shock gas must radiate efficiently with a cooling length less than the bow size, see § 3.2 of Paper I. This is satisfied for all but the lowest densities (Paper I's Fig. 2).
2. A significant fraction of the shock energy must be radiated by dust. This requires that the post-shock temperature be greater than $10^6$ K, which requires a stream velocity $v_\infty > 200\,{\rm km\,s^{-1}}$ (Draine 1981). This also coincides with the range of shock velocities where the smaller grains will start to be destroyed by sputtering in the post-shock gas.
3. The kinetic energy flux through the shock must be significant, compared with the fraction of the stellar radiation flux that is absorbed and reprocessed by the bow shell.

It turns out that the third condition is the most stringent, so we will consider it in detail. The kinetic energy flux through the outer shock for an ambient stream of density $\rho_\infty$ and velocity $v_\infty$ is

$$F_{\text{kin}} = \tfrac{1}{2}\rho_\infty v_\infty^3 = \tfrac{1}{2}P_{\text{sh}}v_\infty \,, \tag{12}$$

while the stellar radiative energy flux absorbed by the shell is

$$F_{\text{abs}} \approx \tau L/4\pi R_0^2 \,, \tag{13}$$

assuming an absorption optical depth $\tau \ll 1$. The shell pressure in the WBS case can be equated to the ram pressure of the internal stellar wind (see § 2.1 of Paper I), so that the ratio of the two energy fluxes is

$$\frac{F_{\text{kin}}}{F_{\text{abs}}} = \frac{1}{2}\frac{\eta_{\text{w}}}{\tau}\frac{v_\infty}{c} \,. \tag{14}$$

An upper limit to the stellar wind momentum efficiency $\eta_{\text{w}}$ is the shell momentum efficiency $\eta_{\text{sh}}$ that is derived observationally in § 2, where it is found that $\eta_{\text{sh}}/\tau < 30$ for all sources considered. Therefore, for a stream velocity $v_\infty = 200\,\text{km s}^{-1}$, we have $F_{\text{kin}}/F_{\text{abs}} < 0.01$ and the shock-excited dust emission is still negligible. Only in stars with $v_\infty > 1000\,\text{km s}^{-1}$ would the shock emission start to be significant, and such hyper-velocity stars (Brown 2015) do not show detectable bow shocks.

So far, we have only considered the outer shock, but the inner shock that decelerates the stellar wind will have a velocity of $1000\,\text{km s}^{-1}$ to $3000\,\text{km s}^{-1}$ and therefore might have a significant kinetic energy flux by eq. (14). However, the stellar wind from hot stars will be free of dust,[2] so that it would be necessary for the stellar wind protons to cross the contact/tangential discontinuity and deposit their energy in the dusty plasma of the shocked ambient stream in order for this source of energy to contribute to the grain emission. This is not possible because the Larmor radius (see § 5 of Paper II) of a $3000\,\text{km s}^{-1}$ proton in a $1\,\mu\text{G}$ field is only $3 \times 10^{10}$ cm, which is millions of times smaller than typical bow sizes. The magnetic field in the outer shell is unlikely to be smaller than $\approx n^{1/2}\mu\text{G}$, given that Alfvén speeds of $2\,\text{km s}^{-1}$ are typical of photoionized regions (cf. Paper II's eq. [40]) and if the density were much lower than $1\,\text{cm}^{-3}$, then the scale of the bow would be commensurately larger anyway. Three-dimensional MHD simulations of bow shocks (Katushkina et al. 2017; Gvaramadze et al. 2018) show that the magnetic field lines are always oriented parallel to the shell, so that high energy particles from the stellar wind would be efficiently reflected in a very thin layer and cannot contribute to grain heating. For the same reason, heat conduction by electrons across the contact discontinuity is also greatly suppressed (Meyer et al. 2017).

# 6    STELLAR WIND MASS-LOSS RATES

Third method used by Gvaramadze et al. (2012), relies on measurements of H II region and bow. Only works for isolated stars.

Mass loss rates - starting from Kobulnicky et al. (2010)

## 6.1    Mass loss determination from the $\tau$–$\eta_{\text{sh}}$ diagram

## 6.2    Mass loss determination method of Kobulnicky et al. (2018)

K18 derive mass loss rates for their sources using a method that is different from the one that we employ in § ??. Both methods are
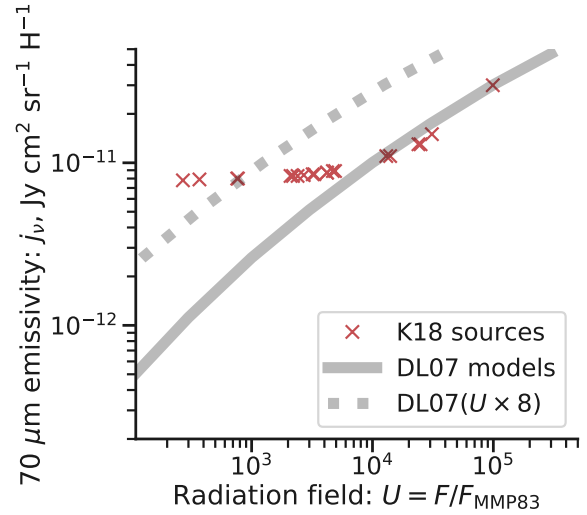
---



**Figure 6.** Discrepancies in $70\,\mu\text{m}$ emissivities that we have identified in K18. Red crosses show the emissivities given in K18's Table 2 as a function of the radiation field $U$, while the solid gray line shows the emissivities that they claim to be using from Draine & Li (2007). The dashed line shows the emissivities that we believe they should have been using, which correct for the marked difference in spectral energy distribution between OB stars and the Galactic interstellar radiation field (see App. 5).

based on determining the stellar wind ram pressure that supports the bow shell, but K18 do so via the following steps:

K1. The line-of-sight mass column through the shell is calculated by combining the peak surface brightness at $70\,\mu\text{m}$, $S_{70}$, with a theoretical emissivity per nucleon, $j_{70}(U)$, from Draine & Li (2007): $\Sigma_{\text{los}} = S_{70}/\bar{m}j_{70}(U)$. This depends on knowledge of the stellar radiation field at the shell: $U \propto L_*/R_0^2$.

K2. The shell density is found from the line-of-sight mass column using an observationally determined "chord diameter", $\ell$, which is assumed to be equal to the depth along the line of sight: $\rho_{\text{sh}} = \Sigma_{\text{los}}/\ell$.

K3. The internal ram pressure is equated to the external ram pressure, which is found by assuming a stream velocity of $30\,\text{km s}^{-1}$ and a compression factor of 4 across the outer shock: $P_{\text{stream}} = 0.25\rho_{\text{sh}} \times (30\,\text{km s}^{-1})^2$.

There are clear parallels but also differences between steps K1–K3 and our own steps P1–P3. Our step P1 depends on the total observed infrared flux of the bow combined with an assumption about the grain opacity at ultraviolet wavelengths, while step K1 depends on the peak brightness at a single wavelength combined with an assumption about the grain emissivity at infrared wavelengths. Our step P2 requires an assumption about the relative thickness of the shell, while step K2 is more directly tied to observations.[3] On the other hand, step K3 makes a roughly equivalent assumption about the shock compression factor,[4] and a further assumption about the

---

[2]  With the exception of Wolf-Rayet colliding wind binary systems (Tuthill et al. 1999; Callingham et al. 2019).

---

[3]  Note that there is a relation between the chord length, $\ell$, and the shell thickness, $h_{\text{sh}}$, but this depends on the planitude, $\Pi$ of the bow shape (Tarango-Yong & Henney 2018): $h_{\text{sh}}/R_0 = \Pi\left(1 - \{1 - [\ell/(2\Pi R_0)]^2\}^{1/2}\right)$.

[4]  In reality, the compression factor may be larger or smaller than 4, depending on the efficiency of the post-shock cooling (see § ??). For instance, for $v = 30\,\text{km s}^{-1}$ as assumed by K18 and $T = 10^4$ K, one has a Mach number
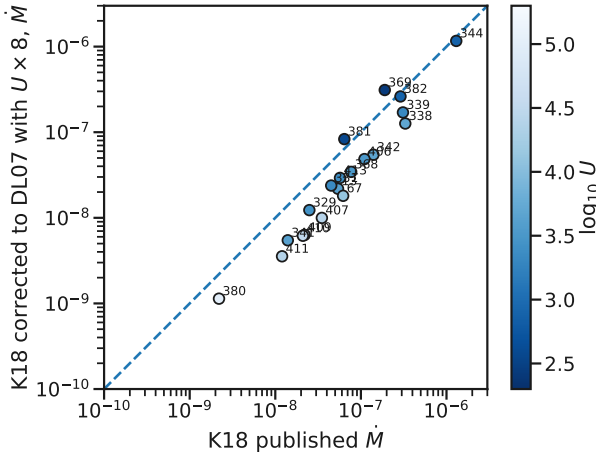
**Figure 7.** Effects on mass-loss determination of correcting the K18 emissivities. The mass-loss rates from Table 2 of K18 are shown on the $x$ axis, while the corrected values are shown on the $y$ axis. Symbols are color coded by the strength of the radiation field, $U$. The corrected mass-loss rates are predominantly lower by a factor of roughly 2.

**Figure 8.** Comparison of the two mass-loss methods: K18 corrected method ($x$ axis) versus our method ($y$ axis). Error bars on the $y$ axis correspond to a factor-three uncertainty in $\eta_{sh}$. Sources for which these error bars overlap with the RBW zone are only upper limits for the wind mass-loss rate, and are indicated by faint symbols.

stream velocity. These assumptions are not necessary for our step P3, but we do need to assume a value for the shell gas temperature.

In principle, both methods are valid and their different assumptions and dependencies on observed quantities and auxiliary parameters provide an important cross check on one another. However, as explained in detail in Appendix 5, the $j_\nu(U)$ relation depends on the shape of the illuminating SED, which means that the Draine & Li (2007) models require modification when applied to grains around OB stars. In addition, when attempting to replicate the K18 values of $j_{70}$ we find that they only follow the Draine & Li (2007) values for $U > 10^4$, tending to a constant value for weaker radiation fields. The situation is summarized in Figure 6, where the values taken directly from Table 2 of K18 are shown by red crosses, the values they claim to be using are shown by the gray solid line (this curve is consistent with that shown in K18 Fig. 2), and the values they *should* have been using are shown by the gray dashed line.

After correcting the 70 μm emissivities in this way, we re-derive the mass loss rates, following the same steps as in K18, which are then used in Figure 9b of § **??**. The difference between these corrected mass-loss rates and those published in K18 is shown in Figure 7. It can be seen that sources with $U \approx 10^3$ (darker shading) are relatively unaffected but that sources with stronger radiation fields (lighter shading) have their mass-loss increasingly reduced, as could be surmised from Figure 6. The average reduction is by a factor of about two.

Finally, in Figure 8 we compare our own mass-loss determinations with the corrected K18 values. The plot symbols are shaded according to the physical size of the bow, $R_0$. It is apparent that the two methods are broadly in agreement on average, but there is considerable dispersion for individual objects, with only a weak correlation between the results of the two techniques (Pearson correlation coefficient $r = 0.67$). Interestingly, the smaller bows (darker shadin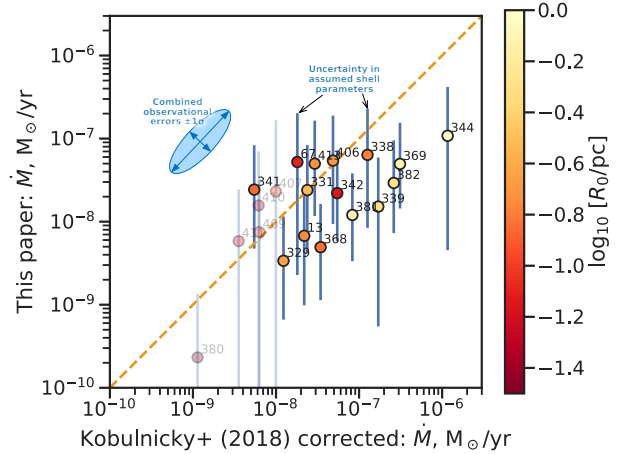g) show much better agreement than the larger bows (lighter shading). The five bows with $R_0 > 0.4$ pc (339, 344, 369, 381, 382) show a difference of nearly an order of magnitude, in the sense that our method consistently predicts lower mass-loss rates than K18. For a further five of the sources (380, 407, 409, 410, 411), our method gives only an upper limit to the wind mass-loss rate if one assumes a factor-three uncertainty in $\eta_{sh}$, and these bows are among the smallest in the sample, all with $R_0 < 0.1$ pc.

Source 342 is anomalous in both methods.

Evidence for small grains around Arches cluster near Galactic center (Hankins et al. 2017)

Different scenarios for producing velocities: dynamic ejection from young clusters (Hoogerwerf et al. 2001; Oh & Kroupa 2016) produce high velocities, dissolution of binary systems following core-collapse SN (Renzo et al. 2018) tend to produce lower velocities for the unbound MS companion (walkaways, slower than 30 km/s). Also, champagne flows have low velocities.

How different regions of the Π–Λ plane are populated. Bottom-right quadrant hard to get to (except for standing wave oscillations), but may be due to finite shell thickness, which (for low Mach number) will be more apparent in the wings, which might decrease Λ more than Π. Fact that thin-shell solutions should trace the contact discontinuity, but in some cases it may be only the inner or the outer shell that is visible.

Justification for standing waves: Fig. 3 of Meyer et al. (2016) shows a time sequence of thin-shell instability, which looks a bit like a standing wave. But much larger amplitude than we are considering.

Deviations from axisymmetry as an alternative to oscillations.

### 6.3 Diagnosing bow type from shell emission profile

Given that the predicted shell density profile varies between wind-supported and radiation-supported bows (Paper I) it is worth considering whether it may be possible to use observed emission profiles to distinguish between the two.

of $\mathcal{M}_0 = 2.63$ and a compression factor of 2.8 for a non-radiative shock (by eq. [**??**]) or a factor of $\mathcal{M}_0^2 = 6.9$ for a strongly radiative one.
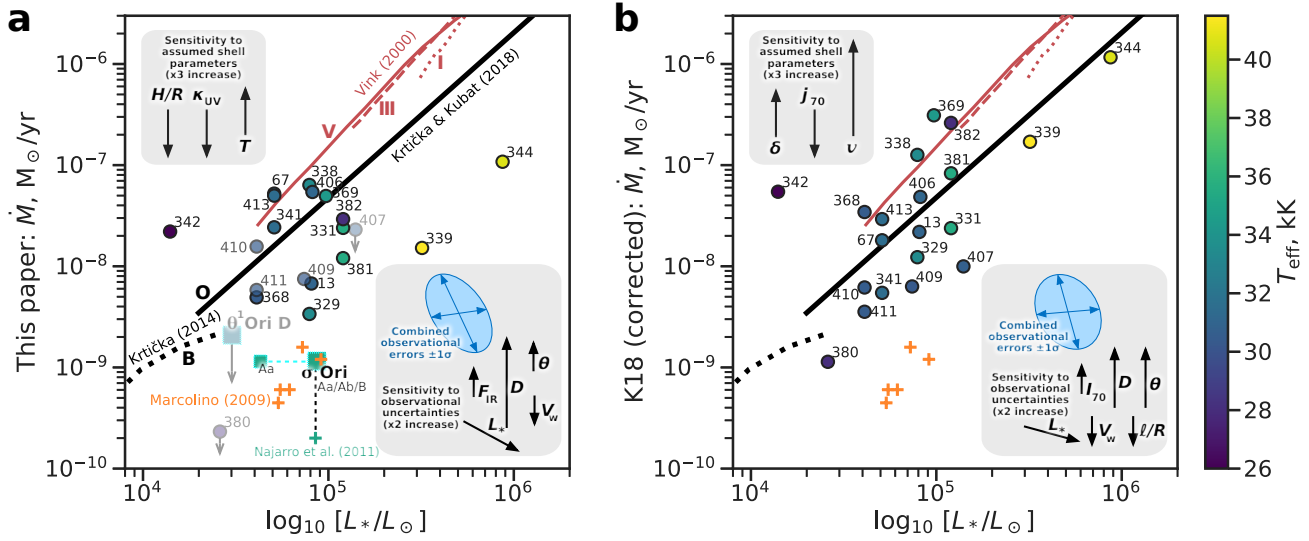
**Figure 9.** Wind mass-loss rates as a function of stellar luminosity, derived from (a) our trapped energy/momentum method and (b) the grain emissivity method of Kobulnicky et al. (2018), with corrections as described in our Appendix 6.2. Circle symbols show the sources from K18, colored according to the stellar effective temperature (see key at far right). In panel a, squares show two of our additional sources (Tab. 1). Upper limits to the mass loss are given for sources that lie close to the radiation-supported line in Fig. 1, represented by faint symbols and downward-pointing arrows. Sources that lie less than a factor of three above the line have enhanced downward uncertainties and are also shown by slightly fainter symbols. For $\sigma$ Ori, the large symbol corresponds to the sum of the luminosities of the triple OB system Aa, Ab, and B (Simón-Díaz et al. 2015), while the small symbol corresponds to the luminosity of only the most massive component Aa. Lines show the predictions of stellar wind models: red lines are the commonly used recipes from Vink et al. (2000) for dwarfs (solid), giants (dashed), and supergiants (dotted), while black lines show eq. (11) of Krtička & Kubát (2017) for O stars (solid) and models of Krtička (2014) for B stars. Orange plus symbols show mass-loss measurements from NUV lines for weak-wind O dwarfs (Marcolino et al. 2009), while the green plus symbol shows the measurement from infrared H recombination lines for $\sigma$ Ori (Najarro et al. 2011). Boxes show the sensitivity of the results to observational uncertainties (lower right) and assumed shell parameters (upper left).

## 6.4 The case of inside-out bows

So far, we have considered the case where the inner source dominates the radiation, while dust is present only in the outer stream, which applies to hot stars interacting with the ISM. However, in the case of cool stars, the inner wind will also be dusty. Examples are the red supergiant (RSG) phase of high-mass evolution, or the asymptotic giant branch (AGB) stage of low/intermediate-mass evolution. In both these cases, it is still the inner source that provides the radiation field. However, not all winds are radiatively driven and in those cases it is conceivable that it is the outer source that dominates the radiation field. An example is the case of photoevaporating protoplanetary disks (proplyds) in the Orion Nebula and other H II regions (O'Dell & Wen 1994). In the proplyds, the inner wind is a thermally driven photoevaporation flow (Henney & Arthur 1998; Henney & O'Dell 1999), while the outer stream is the stellar wind from an O star (García-Arredondo et al. 2001).

## 7 SUMMARY AND CONCLUSIONS

### REFERENCES

Balog Z., et al., 2014, Experimental Astronomy, 37, 129
Beitia-Antero L., Gómez de Castro A. I., 2017, MNRAS, 469, 2531
Brand J., Blitz L., 1993, A&A, 275, 67
Brown W. R., 2015, ARA&A, 53, 15
Callingham J. R., Tuthill P. G., Pope B. J. S., Williams P. M., Crowther P. A., Edwards M., Norris B., Kedziora-Chudczer L., 2019, Nature Astronomy, 3, 82

Desert F.-X., Boulanger F., Puget J. L., 1990, A&A, 237, 215
Draine B. T., 1981, ApJ, 245, 880
Draine B. T., Li A., 2001, ApJ, 551, 807
Draine B. T., Li A., 2007, ApJ, 657, 810
Duley W. W., 1973, Ap&SS, 23, 43
Engelbracht C. W., et al., 2007, PASP, 119, 994
Fairlamb J. R., Oudmaijer R. D., Mendigutía I., Ilee J. D., van den Ancker M. E., 2015, MNRAS, 453, 976
Ferland G. J., et al., 2013, Rev. Mex. Astron. Astrofis., 49, 137
Ferland G. J., et al., 2017, Rev. Mex. Astron. Astrofis., 53, 385
Fitzpatrick E. L., Massa D., 2007, ApJ, 663, 320
Gaia Collaboration et al., 2016, A&A, 595, A1
Gaia Collaboration et al., 2018, A&A, 616, A1
García-Arredondo F., Henney W. J., Arthur S. J., 2001, ApJ, 561, 830
Giard M., Bernard J. P., Lacombe F., Normand P., Rouan D., 1994, A&A, 291, 239
Gvaramadze V. V., Langer N., Mackey J., 2012, MNRAS, 427, L50
Gvaramadze V. V., Alexashov D. B., Katushkina O. A., Kniazev A. Y., 2018, MNRAS, 474, 4421
Habing H. J., 1968, Bull. Astron. Inst. Netherlands, 19, 421
Hankins M. J., Lau R. M., Morris M. R., Herter T. L., 2017, ApJ, 837, 79
Hawley S. A., 1978, ApJ, 224, 417
Henney W. J., Arthur S. J., 1998, AJ, 116, 322
Henney W. J., Arthur S. J., 2019a, arXiv e-prints, 1903.03737 MNRAS submitted (Paper I)
Henney W. J., Arthur S. J., 2019b, MNRAS, submitted (Paper II)
Henney W. J., O'Dell C. R., 1999, AJ, 118, 2350
Hoang T., Tram L. N., Lee H., Ahn S.-H., 2018, arXiv,
Hoogerwerf R., de Bruijne J. H. J., de Zeeuw P. T., 2001, A&A, 365, 49
Katushkina O. A., Alexashov D. B., Izmodenov V. V., Gvaramadze V. V., 2017, MNRAS, 465, 1573

Kobulnicky H. A., Gilbert I. J., Kiminki D. C., 2010, ApJ, 710, 549

Kobulnicky H. A., et al., 2016, ApJS, 227, 18

Kobulnicky H. A., Schurhammer D. P., Baldwin D. J., Chick W. T., Dixon D. M., Lee D., Povich M. S., 2017, AJ, 154, 201

Kobulnicky H. A., Chick W. T., Povich M. S., 2018, ApJ, 856, 74

Krtička J., 2014, A&A, 564, A70

Krtička J., Kubát J., 2017, A&A, 606, A31

Lebouteiller V., Bernard-Salas J., Whelan D. G., Brandl B., Galliano F., Charmandaris V., Madden S., Kunth D., 2011, ApJ, 728, 45

Lee E. J., Murray N., Rahman M., 2012, ApJ, 752, 146

Luri X., et al., 2018, A&A, 616, A9

Marcolino W. L. F., Bouret J.-C., Martins F., Hillier D. J., Lanz T., Escolano C., 2009, A&A, 498, 837

Martins F., Schaerer D., Hillier D. J., 2005, A&A, 436, 1049

Mathis J. S., Mezger P. G., Panagia N., 1983, A&A, 128, 212

Matzner C. D., 2002, ApJ, 566, 302

Meyer D. M.-A., van Marle A.-J., Kuiper R., Kley W., 2016, MNRAS, 459, 1146

Meyer D. M.-A., Mignone A., Kuiper R., Raga A. C., Kley W., 2017, MNRAS, 464, 3229

Najarro F., Hanson M. M., Puls J., 2011, A&A, 535, A32

Nieva M.-F., 2013, A&A, 550, A26

O'Dell C. R., 2001, AJ, 122, 2662

O'Dell C. R., Wen Z., 1994, ApJ, 436, 194

Ochsendorf B. B., Tielens A. G. G. M., 2015, A&A, 576, A2

Ochsendorf B. B., Cox N. L. J., Krijt S., Salgado F., Berné O., Bernard J. P., Kaper L., Tielens A. G. G. M., 2014, A&A, 563, A65

Oh S., Kroupa P., 2016, A&A, 590, A107

Pogodin M. A., Malanushenko V. P., Kozlova O. V., Tarasova T. N., Franco G. A. P., 2006, A&A, 452, 551

Quireza C., Rood R. T., Balser D. S., Bania T. M., 2006a, ApJS, 165, 338

Quireza C., Rood R. T., Bania T. M., Balser D. S., Maciel W. J., 2006b, ApJ, 653, 1226

Renzo M., et al., 2018, arXiv, 1804.09164

Robberto M., et al., 2005, AJ, 129, 1534

Salgado F., et al., 2012, ApJ, 749, L21

Salgado F., Berné O., Adams J. D., Herter T. L., Keller L. D., Tielens A. G. G. M., 2016, ApJ, 830, 118

Schlafly E. F., et al., 2016, ApJ, 821, 78

Simón-Díaz S., et al., 2015, ApJ, 799, 169

Smith N., Bally J., Shuping R. Y., Morris M., Kassis M., 2005, AJ, 130, 1763

Spitzer L., 1978, Physical processes in the interstellar medium. New York: Wiley-Interscience

Stark A. A., 1984, ApJ, 281, 624

Sternberg A., Hoffmann T. L., Pauldrach A. W. A., 2003, ApJ, 599, 1333

Tarango-Yong J. A., Henney W. J., 2018, MNRAS, 477, 2431

Tielens A. G. G. M., Hollenbach D., 1985, ApJ, 291, 722

Tjin A Djie H. R. E., van den Ancker M. E., Blondel P. F. C., Shevchenko V. S., Ezhkova O. V., de Winter D., Grankin K. N., 2001, MNRAS, 325, 1441

Tuthill P. G., Monnier J. D., Danchi W. C., 1999, Nature, 398, 487

Vink J. S., de Koter A., Lamers H. J. G. L. M., 2000, A&A, 362, 295

Weingartner J. C., Draine B. T., 2001, ApJ, 548, 296

Xie Y., Ho L. C., Li A., Shangguan J., 2018, ApJ, 867, 91

van Leeuwen F., 2007, A&A, 474, 653

**Table A1.** Propagation of observational uncertainties to derived quantities

| $x_i$ | $\sigma_{x_i}$ | $J_{x_i}(\tau)$ | $J_{x_i}(\eta_{sh})$ | $J_{x_i}(\dot{M})$ | $J_{x_i}(\dot{M}_{K18})$ | $J_{x_i}(L_*)$ |
|---|---|---|---|---|---|---|
| $D$ | 0.08 | 2 | 3 | 3 | 2 | 0 |
| $L_*$ | 0.18 | −1 | −2 | −1 | −0.5 | 1 |
| $F_{IR}$ | 0.12 | 1 | 1 | 1 | 0 | 0 |
| $I_{70}$ | 0.12 | 0 | 0 | 0 | 1 | 0 |
| $\theta$ | 0.11 | 0 | 1 | 1 | 2 | 0 |
| $\ell/R$ | 0.08 | 0 | 0 | 0 | −1 | 0 |
| $V_w$ | 0.18 | 0 | 0 | −1 | −1 | 0 |

**Table A2.** Variance–covariance matrix $C_{k,k'}$ for derived quantities

| | $\tau$ | $\eta_{sh}$ | $\dot{M}$ | $\dot{M}_{K18}$ | $L_*$ |
|---|---|---|---|---|---|
| $\tau$ | 0.0724 | 0.1176 | 0.0852 | 0.0418 | −0.0324 |
| $\eta_{sh}$ | 0.1176 | 0.2137 | 0.1489 | 0.095 | −0.0648 |
| $\dot{M}$ | 0.0852 | 0.1489 | 0.1489 | 0.1112 | −0.0324 |
| $\dot{M}_{K18}$ | 0.0418 | 0.095 | 0.1112 | 0.1353 | −0.0162 |
| $L_*$ | −0.0324 | −0.0648 | −0.0324 | −0.0162 | 0.0324 |

## APPENDIX A: COVARIANCE OF DERIVED QUANTITIES FROM PROPAGATION OF OBSERVATIONAL UNCERTAINTIES

Even though errors in the fundamental observed quantities, $x_i$, are assumed independent,[5] errors in the derived quantities, $f_k(x_1, x_2, \dots)$, will not necessarily be so. For the purposes of this paper:

$$x_i \in \{D;\ L_*;\ F_{IR};\ I_{70};\ \theta;\ \ell/R;\ V_w\} \qquad (A1)$$

$$f_k \in \{\tau;\ \eta_{sh};\ \dot{M};\ \dot{M}_{K18};\ L_*\}\ . \qquad (A2)$$

Note that $L_*$ appears in both lists because we use it as a graph axis in Figure 9. For the case where each $f_k$ is a simple product of powers of the $x_i$, the propagation of errors reduces to linear algebra of log quantities. This is exactly true for $\tau$ and $\eta_{sh}$, but only approximately so for $\dot{M}$ and $\dot{M}_{K18}$.[6] We define $J_{x_i}(f_k)$ as the elements of the Jacobian matrix of logarithmic derivatives $d \ln f_k / d \ln x_i$, which are given for our quantities in Table A1. Then, the elements of the variance–covariance matrix for the derived parameters are

$$C_{k,k'} = \sum_i J_{x_i}(f_k)\, \sigma_{x_i}^2\, J_{x_i}(f_{k'})\,, \qquad (A3)$$

where the $\sigma_{x_i}$ are the rms dispersions in $x_i$, measured in dex. In Figure A1 we give example python code for calculating this matrix, using the $\sigma_{x_i}$ derived in § 3.2.1–3.2.5 for the K18 sources (second column of Tab. A1), with results given in Table A2. It can be seen that many of the off-diagonal elements are of similar magnitude to the diagonal elements, which is an indication of significant correlations between the errors in the different parameters.

For any particular pair of derived quantities, $f_m$ and $f_n$, one can find the *error ellipse* that characterises the projection of observational errors onto the $f_m$–$f_n$ plane. The ellipse is characterized by standard deviations along major and minor axes, $\sigma_a$, $\sigma_b$, together with the angle $\theta_a$ between the $f_m$ axis and the ellipse major axis. These are given via the eigenvalues and eigenvectors of the relevant $2 \times 2$

---

[5] It is of course true that $F_{IR}$ and $I_{70}$ are not completely independent from one another, but this does not matter since we consider only derived quantities that are a function of one or the other, not both.

[6] For $\dot{M}$ it is true for $\eta_{sh} \gg 1.25\tau$ and for $\dot{M}_{K18}$ it is true in the limit that the grain emissivity can be expressed as a power law in $U$.

**Table A3.** Error ellipse parameters for particular pairs of derived quantities

| $f_m$ | $f_n$ | $\sigma_a$ | $\sigma_b$ | $\theta_a, °$ | Figure |
|-------|-------|------------|------------|---------------|--------|
| $\tau$ | $\eta$ | 0.529 | 0.077 | 60.5 | 1 |
| $L_*$ | $\dot{M}$ | 0.397 | 0.155 | $-75.5$ | 9a |
| $L_*$ | $\dot{M}_{K18}$ | 0.371 | 0.173 | $-81.3$ | 9b |
| $\dot{M}_{K18}$ | $\dot{M}$ | 0.503 | 0.175 | 46.7 | 8 |

```
import numpy as np
sig = np.diag([0.08, 0.18, 0.12, 0.12, 0.11, 0.08, 0.18])
J = np.array([
    [2, -1, 1, 0, 0, 0, 0],
    [3, -2, 1, 0, 1, 0, 0],
    [3, -1, 1, 0, 1, 0, -1],
    [2, -0.5, 0, 1, 2, -1, -1],
    [0, 1, 0, 0, 0, 0, 0]
])
C = J @ sig**2 @ J.T
```

**Figure A1.** Snippet of Python code that calculates the covariance matrix of Table A2. The last line implements equation (A3) by a triple matrix product of the Jacobian matrix J, the square of a diagonal matrix of observational standard deviations sig, and the transpose of J.

submatrix of the covariance matrix:

$$\sigma_a^2 = \frac{1}{2}\left\{ C_{m,m} + C_{n,n} + \left[ \left( C_{m,m} + C_{n,n} \right)^2 - 4C_{m,n}^2 \right]^{1/2} \right\} \quad \text{(A4)}$$

$$\sigma_b^2 = \frac{1}{2}\left\{ C_{m,m} + C_{n,n} - \left[ \left( C_{m,m} + C_{n,n} \right)^2 - 4C_{m,n}^2 \right]^{1/2} \right\} \quad \text{(A5)}$$

$$\theta_a = \frac{1}{2} \arctan\left( \frac{2C_{m,n}}{C_{m,m} - C_{n,n}} \right) . \quad \text{(A6)}$$

For instance, Table A3 shows the resultant error ellipse parameters (shown in blue on the respective graphs) for the relations plotted in Figures 1, 9ab, and 8.

This paper has been typeset from a TEX/LATEX file prepared by the author.